Extreme Mechanics Letters 81 (2025) 102413

Contents lists available at ScienceDirect

Extreme Mechanics Letters

journal homepage: www.elsevier.com/locate/eml

Self-locking and stability of the bowline knot

Bastien F.G. Aymon [a,b], Fani Derveni [a,c], Michael Gomez [a,d], Jérôme Crassous [e,f], Pedro M. Reis [a,*]

[a] Flexible Structures Laboratory, Institute of Mechanical Engineering, École Polytechnique Fédérale de Lausanne (EPFL), 1015 Lausanne, Switzerland
[b] Department of Mechanical Engineering, Massachusetts Institute of Technology, Cambridge, MA 02138, USA
[c] Scalable MetaStructures Laboratory, School of Civil and Environmental Engineering, Cornell University, Ithaca, NY 14853, USA
[d] Department of Engineering, King's College London, Strand, London, WC2R 2LS, United Kingdom
[e] University of Rennes, CNRS, IPR (Institut de Physique de Rennes) - UMR 6251, F-35000 Rennes, France
[f] PMMH, CNRS, ESPCI Paris, Université PSL, Sorbonne Université, Université Paris Cité, F-75005 Paris, France

ARTICLE INFO

Keywords:
Physical knots
Rod mechanics
Friction
Mechanical testing
Numerical simulations

ABSTRACT

We investigate the self-locking of the bowline knot through numerical simulations, experiments, and theoretical analysis. Specifically, we perform two complementary types of simulations using the 3D finite-element method (FEM) and a reduced-order model based on the discrete-element method (DEM). For the FEM simulations, we develop a novel mapping technique that automatically transforms the centerline of the rod into the required knot topology prior to loading. In parallel, we conduct experiments using a nearly inextensible elastic rod tied into a bowline around a rigid cylinder. One end of the rod is pulled to load the knot while the other is left free. The measured force–displacement response serves to validate both the FEM and DEM simulations. Leveraging these validated computational frameworks, we analyze the internal tension profile along the rod's centerline, revealing that a sharp drop in tension concentrates around a strategic locking region, whose geometry resembles that observed in other knot types. By considering the coupling of tension, bending, and friction, we formulate a theoretical model inspired by the classic capstan problem to predict the stability conditions of the bowline, finding good agreement with our FEM and DEM simulations. Our methodology and findings offer new tools and insights for future studies on the performance and reliability of other complex knots.

1. Introduction

The bowline knot, often nicknamed the '*king of the knots*,' is so fundamental to maritime operations that Clifford Ashley states [1]: '*A sailor seldom uses another loop knot aboard ship*.' The bowline is popular, robust, and offers an intuitive tying method (Fig. 1**a**), passed down through generations via the mnemonic: '*The rabbit comes out of the hole, runs around the tree, and goes back in the hole*.' A bowline may be readily attached to a mooring post, cringles in a sail, or even used as an emergency rescue harness around the waist. The bowline creates a secure, non-slip loop at the end of a rope (Fig. 1**b**), forming a *self-locking structure* that can be easily untied even after bearing heavy loads. This self-locking mechanism is not unique to the bowline and appears in several other knots employed in sailing and climbing, including the sheepshank, the double fisherman's knot, the alpine butterfly, and perfection loops [1].

While knot theory is well-established in mathematics, particularly in topology [2,3] and geometry [4,5], the mechanics of physical knots remains largely unexplored. Recent mechanics-based studies of some classical knots (*e.g.*, the overhand [6–8], trefoil [9], fisherman's [10], clove hitch [11], surgical [12] and stopper [13] knots) have revealed how the interplay between topology, geometry, elasticity, and friction underlies the performance of these seemingly simple structures. Building on these recent advances, we study the *bowline*; a knot that, despite centuries of use, lacks thorough structural analysis.

Prior studies have largely focused on the mechanics of simpler knots and have not established quantitative mechanical stability criteria. Here, we combine precision experiments, simulations, and theoretical analysis to investigate the mechanics of the bowline, focusing on its self-locking behavior. First, we introduce a novel mapping technique to create initial knotted configurations for finite element method (FEM) simulations. Previous approaches [8,9,12,13] required cumbersome step-by-step knot construction. By contrast, our approach automatically transforms centerline geometry into the desired configuration through optimized 'temporary' displacements, significantly reducing computational time. We validate this framework through experiments on a

* Corresponding author.
E-mail address: pedro.reis@epfl.ch (P.M. Reis).

https://doi.org/10.1016/j.eml.2025.102413
Received 12 September 2025; Received in revised form 18 October 2025; Accepted 19 October 2025
Available online 27 October 2025

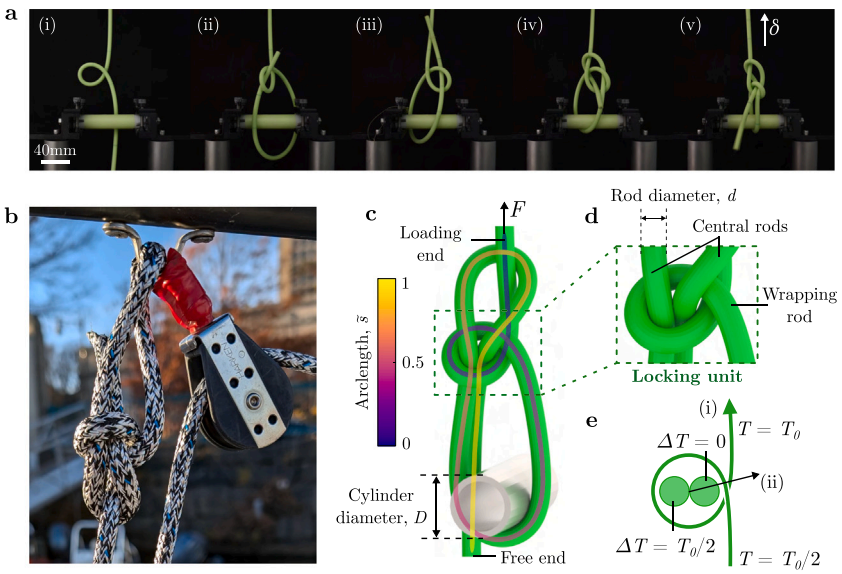

Fig. 1. The bowline knot. **a** Experimental tying sequence. Following step (v), a displacement δ, at constant velocity, v, is imposed at the top end. **b** Example of a bowline knot in practice: a pulley system on a boat's sail. **c** Geometry and primary features of the bowline. **d** Close-up and **e** schematic of the locking unit, with tension values marked at specific locations. The bowline can unravel via either the sliding of (i) the wrapping rod or (ii) the central rods.

nearly inextensible elastomeric rod and compare these results to discrete element method (DEM) simulations for complementary insights. Examining the tension profile along the rod centerline reveals that most force drop localizes around a strategic locking region. This motivates an analytical stability criterion based on the classic capstan problem, considering the interplay between frictional, axial, and bending forces. Finally, this criterion is tested using DEM and FEM results. Our framework provides a foundation for quantitatively investigating the stability of more complex physical knots.

2. Definition of the problem

We consider the bowline knot (see schematic in Fig. 1**c**) obtained by tying a rod of length L and diameter d=2r around a rigid cylinder of diameter D. First, a small loop (the '*rabbit hole*') is formed in the portion of the rod above the cylinder (Fig. 1**a**,i). Next, the rod's free end (the '*rabbit*') is passed under the cylinder and then upward through this loop (Fig. 1**a**,ii). The free end is then routed around the upper segment of the rod (the '*tree*'; Fig. 1**a**,iii) before being guided back down through the loop (Fig. 1**a**,iv). Finally, the knot is tightened by pulling the upper rod segment (Fig. 1**a**,v). An upward displacement, δ, is applied quasi-statically at the loading (upper) end of the rod; the corresponding tightening force is F. The lower end of the rod is free. The normalized arclength along the centerline, s/L=$\tilde{s} \in [0, 1]$, starts at the loading end and finishes at the free end.

The key feature of the bowline knot we seek to investigate is its *locking unit*: the region where a 'wrapping rod' segment loops around two central rod segments (Fig. 1**d**). The importance of this locking unit is evidenced by the fact that a bowline under tension will remain stable if the large loop formed by the central rods is cut, provided that the locking unit is undisturbed (see Supplementary Video 1). We aim to understand how this locking unit contributes to the bowline's self-locking and overall stability. We also assess the capacity of reduced-order models — including DEM simulations of elastic rods and simpler analytical frameworks — to accurately capture the complex mechanics of the bowline.

3. Methods - numerical simulations: FEM and DEM

Several analytical models for elastic knots have been developed [6,7], though they tend to focus on *loose* configurations. By contrast, *tight* physical knots, where bending curvatures are comparable to the rod diameter, are more relevant to applications but call for complex simulations. Our group recently introduced a general strategy to simulate tight knots in 3D FEM [8]. This framework was subsequently used to simulate a variety of tight elastic knots [8,9,13], and extended to incorporate elasto-plasticity, which is relevant for knots in polymeric surgical filaments [12].

State-of-the-art 3D FEM simulations of knots are time-consuming and cumbersome. The first important step in setting up an FEM model for tight knots is obtaining the appropriate topology in a loose configuration prior to loading. Existing approaches for doing so involve a series of carefully chosen tying sub-steps [8] that are highly specific to the chosen knot. Extensive trial and error is required to ensure that the simulation converges in a reasonable number of steps and the final configuration looks as desired. These computational challenges are especially problematic for the bowline knot, since its topology is considerably more intricate than previously investigated knots (*e.g.*, overhand, trefoil, clove hitch).

Reduced-order models based on the Discrete Elastic Rod (DER) method [14–18] are another emerging tool to simulate the mechanics of elastic knots [10]. These computational frameworks are significantly more efficient than 3D FEM, though they neglect cross-section deformations, which can be significant for tight knots where large contact pressures occur. Indeed, Grandgeorge et al. [19] have shown that cross-sectional deformation can occur in the canonical case of two elastic filaments in tight orthogonal contact. Still, it is unclear to what extent cross-sectional deformations influence the large-scale mechanical response of tight knots.

In light of the above, we introduce a novel *mapping technique* that automatically ties an initially straight rod into any desired knot shape in 3D FEM, orders of magnitude faster than existing strategies. We describe the implementation of this mapping technique into a commercial FEM software. Finally, we also employ a DEM simulation framework developed recently for frictional fibers [20], which assumes rigid rod cross-sections.

3.1. A centerline-displacement mapping for elastic knots

In this section, we outline the mapping technique we used to set up the initial configuration of the bowline for FEM simulations; additional

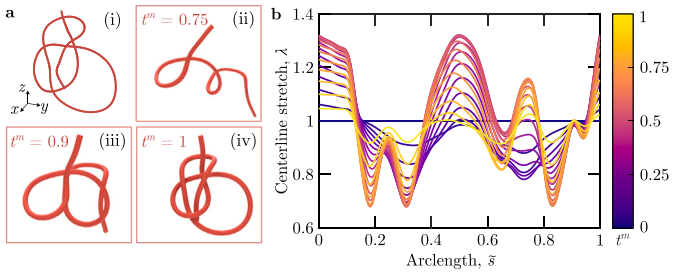

Fig. 2. Mapping technique for initial configuration of the FEM simulations. **a** (i) 'Raw' curve (before Laplacian smoothing is applied) of a loose bowline knot, hand-drawn using Blender. (ii)-(iv) Snapshots of the rod taken from the FEM model along different instances of the mapping iteration time, t^m. Contact is momentarily turned off during this phase. **b** Centerline stretch, λ, as a function of the normalized rod arclength, $\bar{s}$. Curves are color-coded by the mapping time, t^m. The centerline stretch is measured relative to the straight, undeformed configuration; λ=1 corresponds to an inextensible mapping of the straight rod.

details are provided in the Supplementary Information (S.I., Section S1).

Our method utilizes a displacement mapping function designed to minimize stretching along the centerline during the mapping phase, facilitating convergence in the FEM solver. First, as shown in Fig. 2**a**(i), we hand-draw a space curve with the desired topology of the bowline using a non-uniform rational B-spline (NURBS) curve in Blender [21], avoiding the limitations of mathematical parameterizations [3] or experimental measurements (*e.g.*, using X-ray tomography). Subsequently, we discretize the resulting curve into vertices and define a uniform mesh size, h, along the centerline, whose integral yields the rod length L. Local curvature artifacts arising from the hand-drawn data are mitigated by applying uniform Laplacian smoothing; see S.I. Section S1 for details. The resulting smoothed coordinates are imported into MATLAB and scaled uniformly to match the rod length (L=600 mm) used in the experiments (Section 4). Hereafter, we denote these final scaled and smoothed coordinates as $\mathbf{x}_i$.

Given the mesh size h, we define the displacement between the initial and knotted configurations at each vertex as $\mathbf{u}_i=\mathbf{x}_i-\mathbf{X}_i$, where $\mathbf{X}_i=ih\mathbf{e}_z$ corresponds to the coordinates in the straight, undeformed rod. Direct application of this displacement field in FEM typically leads to extreme intermediate deformations and convergence issues (see Fig. S1). To circumvent these issues, we introduce *temporary displacements*, which are optimized to minimize intermediate stretches. We determine the optimal coefficients of the displacement mapping function used for this purpose via an iterative optimization process, minimizing the maximum centerline stretch, $\Lambda_{\max}$, until a desired threshold ($|\Lambda_{\max}-1|<0.3$) is reached. This approach is applicable to a wide range of knots for which a smooth target centerline can be specified.

3.2. Finite-element simulations

We perform finite element simulations using Abaqus 6.23 (Simulia; 2023). The displacement mapping function described above is applied to all centerline nodes of an initially straight rod via a displacement boundary condition in Abaqus/Standard (Fig. 2**a**). We use a custom `UDISP` user subroutine to overcome Abaqus' limitation in handling time- and node-dependent displacement boundary conditions. Contact is disabled during this initial step. As shown in Fig. 2**b**, stretching remains low throughout the mapping because of the temporary displacements, guaranteeing convergence of the FEM solver. All subsequent steps are run in Abaqus using a nonlinear dynamic-implicit analysis.

At the end of the mapping phase, contact is activated using normal penalty forces and a Coulomb friction model. The loose knot is then relaxed with both ends fixed until equilibrium is reached. A controlled force or displacement is finally applied at its loading end, depending on the scenario under consideration. In both cases, loads are applied sufficiently slowly (typical velocity $v/d\approx0.67\ \mathrm{s}^{-1}$) to ensure negligible dynamic effects. For experimental validation (Section 5), self-weight is included using g=9.81 m s^{-2} for gravitational acceleration.

To simulate the combined Nitinol-elastomer rods used in our experiments (Section 4), the rod centerline is meshed using T3D2 linear truss elements ($h/L=1.67\times10^{-3}$) while the elastomeric bulk of the rod uses C3D8H linear brick elements (44 elements per cross-section), as in previous studies [8,9,13]. The material properties are chosen to match the experiments. The addition of Nitinol to the centerline of the experimental elastomeric rod results in a 14% increase in bending stiffness compared to the monolithic elastomeric rod (see discussion in Section 4); the Young's modulus of VPS in the simulations is increased accordingly. The horizontal rigid cylinder around which the knot is tied is modeled as an analytical rigid shell with diameter D=20 mm, as in experiments.

The typical FEM computational time to obtain the initial loose knot topology on a workstation using 15 cores (Intel Xeon E5-2670 2.30 GHz) is 14 min, which is a significant improvement compared to the 60 h reported in a previous study for the tying and loading of an overhand knot [8].

3.3. Discrete-element simulations

In parallel with the FEM simulations, we conduct Discrete Element Method (DEM) simulations using a recently introduced numerical framework [20]. Briefly, the rod is modeled as a set of cylinders of constant circular sections (*i.e.*, no cross-sectional deformations). The elastic stretching, bending, and twisting forces acting on the rod are computed using a Discrete Elastic Rod (DER) model. In particular, the curvature and torsion of the discrete rod are derived from the change in orientation of the local material frames attached to the cylinder axis. The rod-rod or rod-cylinder contacts are modeled using a Cundall-Strack model [22]; at each contact point, the normal contact force $\mathbf{f}_n=[k_n\delta_p-\lambda_n\dot{\delta}_p]\mathbf{n}$, where δ_p is the cylinder interpenetration, $\dot{\delta}_p$ its time derivative, k_n the normal contact stiffness, λ_n a damping coefficient, and $\mathbf{n}$ the common normal to the cylinders at the contact point. The corresponding tangential force between cylinders is computed as $\mathbf{f}_t=k_t\mathbf{u}_t$, with the tangential contact stiffness k_t, and the relative tangential displacement $\mathbf{u}_t$. This displacement is eventually limited to ensure the friction condition $|\mathbf{f}_t|\le\mu_{\mathrm{rr}}|\mathbf{f}_n|$, where μ_{rr} is the rod-rod friction coefficient.

In our DEM simulations, the bowline is modeled as a set of N_c=300 cylinders of simulation length l^*=1 and radius r^*=1.5, with a physical length scale l_0=2 mm (the '0' subscript denotes a physical scale variable). Therefore, the total length of the rod is $L=N_c l^* l_0$=600 mm, and its diameter is $d=2r^*l_0$=6 mm, matching experiments. Taking the axial stiffness of one segment, k_0, for the stiffness scale, the physical scales are $f_0=k_0\,l_0$ for force and $B_0=C_0=k_0\,l_0^3$ for the bending and torsional moduli, respectively.

Due to friction, the geometry of the simulated knots can depend on their preparation history for a given set of applied forces. To ensure reproducibility, we initialize the DEM simulations with a configuration (centerline, twist, contact forces) matching the FEM. We then set μ_{rr}=0 with a frozen centerline and let segments rotate freely to minimize the twisting energy. Subsequently, we set μ_{rr} to the desired value and let the knot relax further prior to applying boundary conditions. We note that Section 6 involves very soft rods that cannot be simulated using FEM; here, the initial shape is obtained by using a rod configuration composed of a succession of straight segments and circular arcs that replicate the bowline topology.

The typical DEM computational time to reach equilibrium from an arbitrary initial shape of the rod is 30 *s* (on a laptop using an Intel Core Ultra 7 165H), nearly 30 times faster than the FEM simulations.

4. Methods - experiments

We performed experiments on an elastomeric rod containing a stiff Nitinol filament at its core. The composite structure is considerably stiffer axially than in bending, qualitatively similar to a rope, while remaining simpler to characterize and model (a rope has an intricate multiscale braided substructure that also involves irreversible deformation due to internal friction). We highlight that our polymer-Nitinol system further decouples axial and bending stiffnesses, while these are correlated in real ropes. The large axial stiffness also allows us to investigate the knot's self-locking ability reliably: without the Nitinol core, the response under tightening would be dominated by axial extension of the unknotted part of the rod. We cast straight, circular rods using vinylpolysiloxane (VPS32, Elite Double 32, Zhermack; Young's modulus E=1.25 MPa, density ρ=1160 kg m^{-3}) inside a straight steel tube (inner diameter d=2r=6 mm, length L=600 mm), as described previously [19]. Following recent work [13], a thin Nitinol wire (radius r_n=0.127 mm, Young's modulus E=75.5 GPa) was suspended along the center of the tube (the mold), with a dead weight (m=200 g) attached at its lower end and laser-cut end guides at each extremity of the mold to ensure that the Nitinol remained straight during casting and curing of the VPS.

The fabricated elastic rods were surface-treated with talcum powder (Millette, Migros) and left to rest for 7 days prior to testing, to stabilize their mechanical properties. This method yields a consistent rod-rod kinetic friction coefficient, measured to be μ_{rr}=0.33 ± 0.04. The rigid cylinder around which the knot is tied (diameter D=20 mm; see Fig. 1**c**) was coated with a thin layer (thickness t=0.3 mm) of VPS32 and, similarly to the rod, was also surface treated with talcum powder; the measured rod-cylinder kinetic friction coefficient is μ_{rc}=0.39 ± 0.02. The frictional behavior of the powder-treated rods and cylinder was systematically characterized following a previously established procedure [19]. Even if small, the increase in bending stiffness due to the Nitinol core was still characterized experimentally and taken into account for simulations, as explained in Section 3.2. Using cantilever tests under self-weight, the VPS-Nitinol rods were measured to have a bending stiffness $(EI)^{\text{exp}}_{\text{VPS/Ni}}$=89.4±8.0 MPa mm^4, whereas bulk VPS rods have $(EI)^{\text{exp}}_{\text{VPS}}$=78.7 ± 7.5 MPa mm^4.

5. Mechanical testing of the bowline knot

Bowline knots were tied on a VPS-Nitinol rod around a rigid cylinder (see Fig. 1**a** and Supplementary Video 2). Tensile experiments were performed using a Universal Testing Machine (Instron 2530, 50 N load cell). We measured the force F as a function of the displacement δ imposed at the loading (upper) end of the rod with a constant velocity of v=4 mm s^{-1} to ensure quasi-static conditions. The applied displacement was stopped at $\delta/r\approx$33, as further deformation risked damaging the rod through delamination between the Nitinol core and VPS. The experimental results described in this section will serve to validate the 3D FEM and DEM simulations presented in Section 3.

In Fig. 3**a**, we present force–displacement curves for the tightening of the bowline knot obtained from experiments, as well as FEM and DEM simulations. To account for variations in the friction coefficient, we considered $\mu_{rr}\in\{0.30, 0.33, 0.37\}$ for the FEM and μ_{rr}=0.37 for DEM (the experimental value is μ_{rr}=0.33 ± 0.04; cf. Section 4). Good agreement is found between experiments and the two types of simulations, validating the numerical models, even if some differences appear at higher applied displacements after locking. The force profile is approximately linear for $\delta/r \lesssim 20$, after which it increases nonlinearly due to self-locking of the knot. We remark that the force behavior past the locking onset is highly dependent on the friction coefficient, with the force at the loading end varying by a factor of two between μ_{rr}=0.30 and μ_{rr}=0.37 at $\delta/r\approx$33. The critical role of friction will be investigated further in Section 6.

Selected snapshots of the FEM tightening procedure along the loading path are presented in Fig. 3**b**. In these snapshots, we also use a colormap to represent the maximum principal strain, ε, which is largest along the wrapping rod within the locking unit, confirming its role in the knot's self-locking ability.

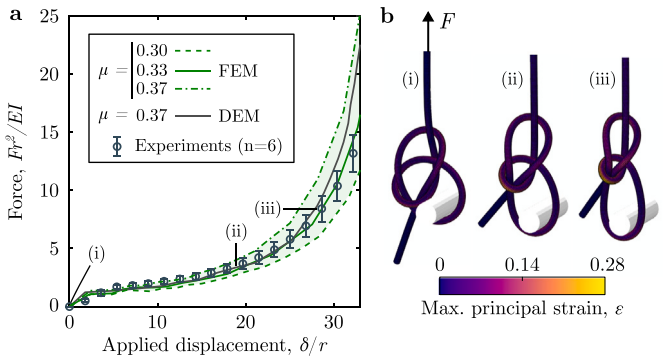

Fig. 3. Experimental validation of the FEM and DEM frameworks. **a** Force–displacement curve of the bowline knot obtained from experiments, as well as from FEM and DEM simulations. The experimental data are averaged over six samples, and error bars represent the standard deviation. The shaded area corresponds to lower and upper bounds for the friction coefficient (μ_{rr}=0.30 and μ_{rr}=0.37, respectively) to account for experimental variation. **b** Snapshots of the knot in FEM at three successive loading steps, (i) to (iii), also represented in **a**. The colormap corresponds to the maximum principal strain, ε.

6. Stability of the bowline knot

Having validated the FEM and DEM simulations against experiments, we proceed to study the bowline's *stability*. First, we analyze the tension profile along the bowline. Then, we leverage this understanding to determine the material properties (friction coefficient, Young's modulus), geometric parameters (rod radius), and loading conditions under which the knot remains stable without unraveling.

6.1. Tension profile along the centerline of the bowline knot

Next, we quantify the tension profile along the bowline's centerline, a quantity that is not available experimentally. Thus, we must rely solely on the validated FEM and DEM simulations to identify which critical portions of the knot are responsible for reducing tension from a high value (at the loading end) to zero (at the free end), which lies at the core of its self-locking ability.

Fig. 4**a** plots the tension profiles along the centerline under an applied load T_0, computed using both the FEM and DEM simulations, for μ_{rr}=0.37. To focus on the mechanics of the locking unit, the cylinder is frictionless in the DEM, and we set μ_{rc}=0.01 in the FEM (not zero, for numerical stability). A relatively small load, $T_0/20$, is applied at the free end, to also aid with numerical stability. In FEM, the tension is obtained by summing nodal forces projected along the centerline direction across each cross-section. In DEM, this tension is directly available. We note that the centerline tension, $T(s)$, is normalized by T_0=$T(s$=0) as $\tilde{T}(s)$=$T(s)/T_0$. As shown in Fig. 4**a**, there are important tension variations along the centerline. First, there is a drop from T_0 to approximately $T_0/2$ in the loop formed by the center rod (at $0.2 \lesssim \tilde{s} \lesssim 0.5$; see Fig. 4**a**,i). This first plateau value of $T_0/2$ is well explained by mechanical equilibrium: since the cylinder is nearly frictionless for this set of simulations, the tension at both extremities of the segment wrapping around the cylinder must be equal to half of the tension applied at the loading end. A second drop in tension from $T_0/2$ to approximately 0 occurs around the wrapping rod region ($0.7 \lesssim \tilde{s} \lesssim 0.9$; see Fig. 4**a**,ii). Importantly, both of these tension drops are directly linked to the locking unit highlighted in Fig. 1**d**.

In addition to these global variations, we observe rapid tension fluctuations along the centerline that differ between FEM and DEM simulations. We attribute these differences to DEM's assumption of undeformable cross-sections, while cross-sections may deform in response to tension and curvature in flexible rods [19,23]. Additionally, the contact points and frictional force histories differ between FEM and

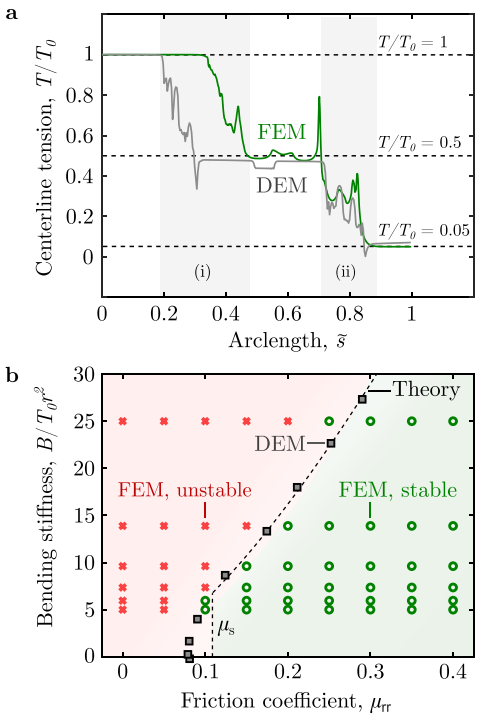

Fig. 4. Tension profile and stability of the bowline. **a** Dimensionless tension profile versus arclength, $\tilde{s}=s/L$. Region (i) corresponds to the tension drop along the wrapping rod and (ii) in the central rod. **b** Stability diagram of the bowline in the parameter space of the normalized bending modulus of the rod versus the rod-rod friction coefficient. The knot is unstable (stable) in the red/left (green/right) regions, respectively. Crosses (circles) represent individual unstable (stable) FEM simulations, respectively. The stability boundaries predicted by DEM and our theory (fitted with α=1.69, β=10.6; cf. Eq. (4b)) are represented by the squares and the dashed line, respectively.

DEM, potentially altering the initial configurations. As described in Section 6.4, these features only weakly affect the bowline's stability.

6.2. Reduced model for the bowline's stability

The findings described above evidence that the bowline's locking performance primarily stems from a 'locking unit' where one rod segment wraps around two core segments. We now analyze this region in more detail. The two observed tension drops appear essential to the bowline's stability, prompting us to develop a simple analytical model.

Wrapping rod slippage condition. The first tension drop identified in Fig. 4**a**(i) is due to the wrapping of a rod segment around two rods forming a central core (see Fig. 1**d**). This structure is similar to a one-turn capstan [23–25]. For a perfectly flexible rod at the onset of sliding, the ratio of tensions at both ends is $T_2/T_1=e^{\mu_{rr}\varphi}$, with φ the total angle swept by the rod; $\varphi\approx 2\pi$ for the one-turn capstan considered here. With T_0 and $T_0/2$ being the tensions acting on both ends of the wrapping rod (see Fig. 1**e**,i), to avoid sliding, the rod-rod friction coefficient must satisfy the following condition:

$$\mu_{rr} \geq \frac{\ln 2}{\varphi} := \mu_s. \tag{1}$$

With $\varphi\approx 2\pi$, sliding is prevented if $\mu_s \gtrsim 0.11$. Since typical friction coefficients of physical ropes and filaments exceed this value of μ_s, the bowline knot rarely experiences this failure mode in practice, provided that the knot is sufficiently tight to ensure full contact along the wrapping region.

Central rods slippage condition. The second tension drop (Fig. 4**a**,ii) occurs along the central rods in the locking unit. The wrapping rod experiences an average tension $T\simeq(T_0+T_0/2)/2=3T_0/4$ (see Fig. 1**e**) that creates normal contact forces acting on the central rods. Approximating the wrapping rod as a perfect string (*i.e.*, no bending stiffness), the normal force $\mathrm{d}N$ acting on a length $\mathrm{d}s$ of contact is $\mathrm{d}N=\kappa T\ \mathrm{d}s$, where κ is the curvature of the wrapping rod. At the onset of sliding, the corresponding frictional force is $\mathrm{d}F_s=\mu_{rr}\mathrm{d}N$. Integrating the frictional force on the wrapping loop yields

$$F_s = \int_{loop} \mu_{rr}\mathrm{d}N = \mu_{rr}T \int_{loop} \kappa \mathrm{d}s \approx 2\pi\mu_{rr}T. \tag{2}$$

If we account for the finite bending stiffness of the wrapping rod, the normal force is no longer constant along contact [8]; thus, Eq. (2) is not applicable and there is no simple theoretical prediction for F_s. The knot strength of the granny knot, whose locking unit exhibits a similar geometry to the bowline's, has been addressed recently [12]. Combining experiments and FEM simulations, these authors showed that the knot strength scales nonlinearly as $\tilde{T}^\alpha$, where $\tilde{T}$ is the pretension of the knot and α=1.56 ± 0.23 is an experimentally determined, albeit robust, exponent. Following this study, we will assume that $F_s \propto \mu_{rr}T^\alpha$, where α is a to-be-determined exponent. The finite bending stiffness regime is expected to occur when tensions are small compared to the characteristic force $B\kappa^2$, where κ is the centerline curvature of the wrapping rod. Combining this phenomenological description with Eq. (2) yields:

$$F_s \approx 2\pi\mu_{rr}T \qquad \text{if } T \gg B\kappa^2, \tag{3a}$$

$$F_s \approx \beta\mu_{rr}T^\alpha(B\kappa^2)^{1-\alpha} \qquad \text{if } T \ll B\kappa^2. \tag{3b}$$

Thus, α encapsulates how finite-stiffness contact departs from the ideal capstan, rather than being a purely empirical exponent. The $(B\kappa^2)^{1-\alpha}$ term arises from dimensional analysis, and β is a dimensionless constant.

Next, we consider both central rods to be a single, equivalent rod of radius $2r$. This simplification preserves the curvature scale while yielding a tractable criterion. We highlight that this approximation is only expected to hold for modest flattening of the rod. Since one of the central rods has almost no tension drop, and the other experiences a drop of approximately $T_0/2$ (see Fig. 1**e**), we take the effective tension drop in the equivalent rod to be $\Delta T=T_0/2$. For this equivalent rod to be secured by the wrapping rod, it must satisfy $\Delta T\leq F_s$. Taking an average tension $T\simeq 3T_0/4$ in the wrapping rod as described above, setting $\kappa=1/2r$, and using Eq. (3a), and Eq. (3b), the stability condition $\Delta T\leq F_s$ becomes:

$$1 \lesssim 3\pi\mu_{rr} \qquad \text{if } T_0 \gg B/r^2, \tag{4a}$$

$$\frac{B}{T_0r^2} \lesssim \left(\frac{3^\alpha\beta}{2}\right)^{\frac{1}{\alpha-1}} \mu_{rr}^{\frac{1}{\alpha-1}} \qquad \text{if } T_0 \ll B/r^2. \tag{4b}$$

For large tensions, Eq. (4a) gives $\mu_{rr}\geq 0.106$, which, coincidentally, is close to the wrapping rod slippage condition described above ($\mu_{rr}\geq\mu_s\approx 0.110$). For low applied tensions ($T_0\ll B/r^2$), Eq. (4b) applies, and the value of μ_{rr} must increase beyond μ_s to prevent slippage of the central rods.

The simple model we just introduced postulates that the mechanics of the bowline's stability can be reduced to that of the simple *locking unit* identified in Section 6.1. Specifically, our model predicts that the bowline becomes unstable and unravels when either (i) the wrapping rod or (ii) the two central rods slip. For both cases, this model offers an explicit stability boundary based on the rod's friction coefficient, radius, and bending stiffness.

6.3. Numerical simulations of the bowline's stability

Next, to test the above analytical model, we conduct a systematic set of DEM and FEM simulations for different values of the normalized bending stiffness, B/T_0r^2, and friction coefficient μ_{rr}.

FEM simulations are performed for each pair of (μ_{rr}, T_0) values: $\mu_{rr} \in [0.0, 0.4]$ with increments of 0.05 and $B/T_0 r^2 \in \{5.0, 6.0, 7.4, 9.1, 13.9, 25.0\}$, yielding a total of 54 simulations. First, a constant tension T_0 is applied at the loading end while fixing the free end, and the knot is allowed to reach static equilibrium. The free end is then released, and a small load $T_0/20$ is applied for numerical stability. The simulation runs until the knot either unravels because the applied load T_0 is too low (unstable) or remains tied, reaching equilibrium (stable).

DEM simulations are performed as follows. A knot is prepared with $\mu_{rr}=0.35$ for a given value of $B/T_0 r^2$. A small load of $T_0/20$ is applied to the free end, similarly to FEM. Then, the friction coefficient is slowly decreased. At some critical value of μ_{rr}, the knot becomes unstable and unravels. The two different failure modes described in Section 6.2 — slippage of the wrapping rod or the central rods — can then be identified with the measurements of the positions of the free ends and the locking unit at the onset of failure.

6.4. Stability diagram of the bowline knot

Fig. 4**b** presents a stability diagram in the $(\mu_{rr}, B/T_0 r^2)$ parameter space, obtained from both FEM and DEM simulations. FEM simulations yield individual points in this space that can be classified as unstable (red crosses) or stable (green circles). The stability boundary predicted by DEM is shown using black squares.

First, we observe that although DEM assumes rigid cross-sections, its stability boundary closely matches FEM, with both predicting that the friction needs to increase to ensure stability when the applied tension is low compared to the characteristic force B/r^2. These findings indicate that cross-sectional deformation is secondary for global stability in this system.

For very flexible rods ($B/T_0 r^2 \ll 1$), the stability occurs around $\mu_s \approx 0.09$, which agrees with the wrapping rod slippage mode in Eq. (1). For stiffer rods, we fit the stability boundary obtained from DEM simulations using Eq. (4b), yielding $\alpha_{fit}=1.69 \pm 0.04$, which is remarkably comparable with the experimental value $\alpha=1.56 \pm 0.23$ measured previously [12]. For the prefactor of the boundary line Eq. (4b), the fitting yields $\beta_{fit}=10.6 \pm 1.0$, in reasonable agreement with the expected crossover between the two functions in Eqs. (3a)–(3b) when $T \sim B\kappa^2$, which predicts $\beta \approx 2\pi$.

Despite the complex topology of the bowline, our simple stability model is able to capture, both qualitatively and quantitatively, the self-locking mechanics of the bowline. The stability threshold given by Eq. Eq. (4b) depends super-linearly $(1/(1-\alpha) \approx 1.7)$ on the friction coefficient. This high sensitivity aligns with the force–displacement results reported in Fig. 3**a**, where the pulling force after self-locking (at $\delta/r \approx 33$) doubles when μ_{rr} is increased by just 23%.

7. Conclusions

Our results uncover a specific *locking unit* in the bowline that is central to the stability of this knot. Analysis of the tension distribution along the rod centerline revealed that most of the tension drop localizes in this region, where a single segment wraps around two others in a geometry reminiscent of a capstan. This observation motivated a simplified capstan-based stability model, which we validated against both FEM and DEM simulations. The good agreement between theory, DEM, and FEM, even though DEM neglects cross-sectional deformations, suggests that simplified models can reliably capture the essential mechanics of tight knots such as the bowline.

More broadly, our study highlights mechanical motifs that extend beyond the bowline and recur across a variety of practical knots. Because similar locking units appear across a wide range of functional knots, the present framework could provide a foundation for identifying general stability criteria that couple topology, elasticity, and friction. While our focus has been on quasi-static behavior and simplified rod models, important open directions for future research include the role of dynamic effects, cyclic loading, and the multiscale structure of real ropes. While our FEM framework already accounts for inertia via a dynamic-implicit step, such studies remain challenging and will require more sophisticated computational tools.

CRediT authorship contribution statement

Bastien F.G. Aymon: Writing – review & editing, Writing – original draft, Visualization, Validation, Software, Methodology, Investigation, Formal analysis, Data curation, Conceptualization. **Fani Derveni:** Writing – review & editing, Validation, Methodology, Investigation, Data curation. **Michael Gomez:** Writing – review & editing, Visualization, Validation, Software, Methodology, Investigation, Formal analysis, Data curation. **Jérôme Crassous:** Writing – review & editing, Visualization, Validation, Software, Methodology, Investigation, Formal analysis, Data curation. **Pedro M. Reis:** Writing – review & editing, Writing – original draft, Visualization, Supervision, Resources, Funding acquisition, Data curation, Conceptualization.

Declaration of competing interest

The authors declare that they have no known competing financial interests or personal relationships that could have appeared to influence the work reported in this paper.

Acknowledgments

We are grateful to Paul Johanns for valuable discussions and support with preliminary experiments, and to Javier Sabater for assistance with the friction-coefficient measurements.

Appendix A. Supplementary data

Supplementary material related to this article can be found online at https://doi.org/10.1016/j.eml.2025.102413.

Data availability

Data will be made available on request.

References

[1] C.W. Ashley, The Ashley Book of Knots, Doubleday, New York, 1944.
[2] D. Rolfsen, Knots and Links, American Mathematical Society, 2003, http://dx.doi.org/10.1090/chel/346.
[3] C.C. Adams, The Knot Book: An Elementary Introduction to the Mathematical Theory of Knots, American Mathematical Society, 2010.
[4] O. Gonzalez, J.H. Maddocks, Global curvature, thickness, and the ideal shapes of knots, Proc. Natl. Acad. Sci. 96 (9) (1999) 4769–4773, http://dx.doi.org/10.1073/pnas.96.9.4769.
[5] M. Carlen, B. Laurie, J.H. Maddocks, J. Smutny, Biarcs, global radius of curvature, and the computation of ideal knot shapes, Ser. Knots Everything (2005) 75–108, http://dx.doi.org/10.1142/9789812703460_0005.
[6] B. Audoly, N. Clauvelin, S. Neukirch, Elastic knots, Phys. Rev. Lett. 99 (16) (2007) http://dx.doi.org/10.1103/physrevlett.99.164301.
[7] M. Khalid Jawed, P. Dieleman, B. Audoly, P.M. Reis, Untangling the mechanics and topology in the frictional response of long overhand elastic knots, Phys. Rev. Lett. 115 (11) (2015) http://dx.doi.org/10.1103/physrevlett.115.118302.
[8] C. Baek, P. Johanns, T.G. Sano, P. Grandgeorge, P.M. Reis, Finite element modeling of tight elastic knots, J. Appl. Mech. 88 (2020) http://dx.doi.org/10.1115/1.4049023.
[9] P. Johanns, P. Grandgeorge, C. Baek, T.G. Sano, J.H. Maddocks, P.M. Reis, The shapes of physical trefoil knots, Extrem. Mech. Lett. 43 (2021) 101172, http://dx.doi.org/10.1016/j.eml.2021.101172.
[10] D. Tong, M. Ibrahim Khalil, M. Justin Silva, G. Wang, B. Khoda, M. Khalid Jawed, Mechanical response of fisherman's knots during tightening, J. Appl. Mech. 91 (3) (2023) http://dx.doi.org/10.1115/1.4063895.
[11] T.G. Sano, P. Johanns, P. Grandgeorge, C. Baek, P.M. Reis, Exploring the inner workings of the clove hitch knot, Extrem. Mech. Lett. 55 (2022) 101788, http://dx.doi.org/10.1016/j.eml.2022.101788.

[12] P. Johanns, C. Baek, P. Grandgeorge, S. Guerid, S.A. Chester, P.M. Reis, The strength of surgical knots involves a critical interplay between friction and elastoplasticity, Sci. Adv. 9 (23) (2023) http://dx.doi.org/10.1126/sciadv.adg8861.

[13] P. Johanns, P.M. Reis, Capsizing due to friction-induced twist in the failure of stopper knots, Extrem. Mech. Lett. 68 (2024) 102134, http://dx.doi.org/10.1016/j.eml.2024.102134.

[14] M. Bergou, M. Wardetzky, S. Robinson, B. Audoly, E. Grinspun, Discrete elastic rods, 2008, pp. 1–12, http://dx.doi.org/10.1145/1399504.1360662, ACM SIGGRAPH 2008 papers.

[15] M.K. Jawed, F. Da, J. Joo, E. Grinspun, P.M. Reis, Coiling of elastic rods on rigid substrates, Proc. Natl. Acad. Sci. 111 (41) (2014) 14663–14668, http://dx.doi.org/10.1073/pnas.1409118111.

[16] D. Tong, A. Choi, J. Joo, M.K. Jawed, A fully implicit method for robust frictional contact handling in elastic rods, Extrem. Mech. Lett. 58 (2023) 101924, http://dx.doi.org/10.1016/j.eml.2022.101924.

[17] W. Huang, Z. Hao, J. Li, D. Tong, K. Guo, Y. Zhang, H. Gao, K.J. Hsia, M. Liu, A tutorial on simulating nonlinear behaviors of flexible structures with the discrete differential geometry (DDG) method, Appl. Mech. Rev. (2025) 1–88, http://dx.doi.org/10.1115/1.4069025.

[18] W.-C. Li, G. Chou, A convex formulation of compliant contact between filaments and rigid bodies, 2025, arXiv:2509.13434.

[19] P. Grandgeorge, C. Baek, H. Singh, P. Johanns, T.G. Sano, A. Flynn, J.H. Maddocks, P.M. Reis, Mechanics of two filaments in tight orthogonal contact, Proc. Natl. Acad. Sci. 118 (15) (2021) http://dx.doi.org/10.1073/pnas.2021684118.

[20] J. Crassous, Discrete-element-method model for frictional fibers, Phys. Rev. E 107 (2) (2023) http://dx.doi.org/10.1103/physreve.107.025003.

[21] B.O. Community, Blender - a 3D Modelling and Rendering Package, Blender Foundation, Stichting Blender Foundation, Amsterdam, 2018.

[22] P.A. Cundall, O.D.L. Strack, A discrete numerical model for granular assemblies, Géotechnique 29 (1) (1979) 47–65.

[23] P. Grandgeorge, T.G. Sano, P.M. Reis, An elastic rod in frictional contact with a rigid cylinder, J. Mech. Phys. Solids 164 (2022) 104885, http://dx.doi.org/10.1016/j.jmps.2022.104885.

[24] L. Euler, Remarques sur l'effet du frottement dans l'equilibre, Memoires de L'Academie Des Sci. de Berl. (1769) 265–278.

[25] J.A. Eytelwein, Handbuch der Statik fester Körper: mit vorzüglicher Rücksicht auf ihre Anwendung in der Architektur, vol. 1, Reimer, 1832.